

SPH modeling of dynamic impact of tsunami bore on bridge piers



Zhangping Wei ^{a,*}, Robert A. Dalrymple ^a, Alexis Hérault ^{b,c}, Giuseppe Bilotta ^c, Eugenio Rustico ^d, Harry Yeh ^e

^a Department of Civil Engineering, Johns Hopkins University, Baltimore, MD 21218, USA

^b Conservatoire National des Arts et Métiers, Paris 75003, France

^c Istituto Nazionale di Geofisica e Vulcanologia, Sezione di Catania, 95123 Catania, Italy

^d Bundesanstalt für Wasserbau, 76187 Karlsruhe, Germany

^e School of Civil & Construction Engineering, Oregon State University, Corvallis, OR 97331, USA

ARTICLE INFO

Article history:

Received 31 March 2015

Received in revised form 9 June 2015

Accepted 13 June 2015

Available online 12 August 2015

Keywords:

Tsunami bore

Bridge piers

Wave–structure interaction

Hydrodynamic force

GPUSPH

Smoothed Particle Hydrodynamics

ABSTRACT

The Smoothed Particle Hydrodynamics (SPH) method is applied to investigate the impact of a tsunami bore on simplified bridge piers in this study. This work was motivated by observations of bridge damage during several recent tsunami events, and its aim is to further the understanding of the dynamic interaction between a tsunami bore and a bridge pier. This study is carried out by simulating a well-conducted physical experiment on a tsunami bore impingement on vertical columns with an SPH model, GPUSPH. The influences of bridge pier shape and orientation on free surface evolution and hydrodynamic loading are carefully examined. Furthermore, the unsteady flow field that is around and in the wake of the bridge pier is analyzed. Finally, GPUSPH is applied to explore the hydrodynamic force caused by the bridge pier blockage, the wave impact on structures, and the bed shear stress around a bridge pier due to a strong tsunami bore.

© 2015 Elsevier B.V. All rights reserved.

1. Introduction

A tsunami disaster is one of the most devastating natural hazards; it not only causes loss of life, but also destroys infrastructure such as buildings and bridges. There were more than 300 bridges washed away during the 2011 Great East Japan Tsunami (Kawashima et al., 2011), and a field investigation in Indonesia after the December 2004 Great Indian Ocean Tsunami also shows that the tsunami caused the collapse of a number of bridges (Saatcioglu et al., 2006). Several modes of bridge failure, e.g., uplift due to buoyancy, washing of superstructures (Kawashima et al., 2011), movement of the abutments and piers, and scouring of foundations (Kawashima and Buckle, 2013), have been observed. Clearly the hydrodynamic loading of tsunamis on bridges, and the dynamic interaction between tsunamis and bridge structures are important for bridge design.

A tsunami is generated by displacement of a substantial volume of water, which then propagates in the form of a long wave in the deep ocean. Once it approaches the shallow water, it undergoes shoaling and may eventually break into a series of bores (e.g., Bryant, 2014). The fluid velocity of tsunami bores during the 2011 Great East Japan

Tsunami reached to 7 m/s (Kawashima et al., 2011; Kawashima and Buckle, 2013). Considering the high-speed flows run over irregular and complex topographies, strong tsunami bores are unsteady in nature.

Owing to the infrequent nature of a tsunami event, it is difficult to conduct experiments in the field, so most of studies on tsunamis interaction with coastal structures utilize physical experiments and numerical simulations. In the laboratory, a solitary wave is often used as a convenient approximation to a tsunami. To further the understanding of physical parameters involved in three-dimensional (3D) tsunami run-up, a series of large-scale physical experiments involving solitary wave run-up a vertical wall and a conical island were conducted at USACE Waterways Experiment Station during 1992 and 1995 (Briggs et al., 1995, 1996). Titov and Synolakis (1995) reported a solitary wave with wave height $A/h = 0.3$ (where A is the solitary wave height, and h is the still water depth) run-up a plane slope. Due to the simple geometry considered in aforementioned experiments, they have been widely used for numerical wave model validation (see, e.g., Weiss et al., 2010; Wei and Jia, 2014; Shadloo et al., 2015). In recent years, complicated laboratory topographies have also been used to study more challenging nearshore tsunami processes, such as tsunami attack of an island (Matsuyama and Tanaka, 2001), tsunami breaking over a 3D shallow reef (Swigler, 2009), and tsunami–debris interaction (Rueben et al., 2014). It is noted that most of these experiments only measure the free surface evolution and time-series of velocity at a

* Corresponding author.

E-mail addresses: zwei@jhu.edu, zwei.coast@gmail.com (Z. Wei), rad@jhu.edu (R.A. Dalrymple), alexis.herault@cnam.fr (A. Hérault), giuseppe.bilotta@ingv.it (G. Bilotta), eugenio.rustico@baw.de (E. Rustico), harry@engr.orst.edu (H. Yeh).

fixed number of gages, and few of them consider the hydrodynamic loading of a tsunami on structures (e.g., hydrodynamic pressure and wave forces).

Ramsden and Raichlen (1990) generated a solitary wave and measured the impact force on a vertical wall. Arnason et al. (2009) measured the hydrodynamic force of a tsunami bore on different configurations (e.g., shape and orientation) of vertical columns; they also collected velocity profiles around/in the wake of structures. It should be pointed out that this set of experiments resembles well a real-life tsunami bore impact on bridge piers, since (1), the generated flow field is unsteady, as observed in real-life tsunami events (e.g., Kawashima et al., 2011); and (2), the ratio of the approaching bore height over the width of vertical columns is close to unity. In reality, this dimensional ratio of tsunami bores over bridge piers was similar to or even larger than unity when the bridge superstructures were washed away by tsunamis (e.g., Kawashima and Buckle, 2013).

In this study, the Smoothed Particle Hydrodynamics (SPH) method is applied to simulate the experiment of Arnason et al. (2009) including the dynamic impact of a tsunami bore on bridge piers. In the past decade, the mesh-free method of SPH has gained popularity for modeling free surface flows, and it has become an alternative to traditional mesh-based methods for modeling coastal waves. Owing to the Lagrangian nature of the SPH method, there is no need to deal with the free surface when it is applied to simulate free surface flows, especially when the surface tension is not important. This property makes it particularly attractive to modeling water waves, e.g., wave propagation over beaches (e.g., Dalrymple and Knio, 2000; Monaghan and Kos, 1999), wave–structure interaction (e.g., Dalrymple and Rogers, 2006; Gómez-Gesteira and Dalrymple, 2004), nearshore rip–current system (Farahani et al., 2013), and turbulent vortical structures due to broken solitary waves (Farahani and Dalrymple, 2014). Furthermore, the SPH method is able to compute the dynamic force on structures directly (see, e.g., Gómez-Gesteira and Dalrymple, 2004). In terms of modeling tsunamis, SPH models have been applied to simulate landslide-generated tsunami (Capone et al., 2010; Rogers and Dalrymple, 2008), and tsunami inundation and run-up (Shadloo et al., 2015; Weiss et al., 2010). Recently, St-Germain et al. (2014) conducted a physical experiment similar to that of Arnason et al. (2009) to measure the hydrodynamic force of a tsunami bore exerted on a square column, and further computed the hydrodynamic force by an SPH model. Although St-Germain et al. (2014) have shown an SPH model has great potential to investigate a tsunami bore impact on a square bridge pier, the coarse particle size that they used (compared with the size used in the current study) is not fine enough to present an accurate and quantitative free surface evolution.

In this work, a high-fidelity SPH model, GPUSPH, is applied to study a tsunami bore impact on bridge piers in a thorough way. The influence of different configurations of bridge piers on free surface evolution and hydrodynamic loading are investigated, and the transient velocity field in the wake of a bridge pier is compared to the measurements of Arnason et al. (2009). Moreover several important issues, e.g., the blockage effect of the bridge pier, wave impingement on different shapes of piers, and the bed shear stress distribution under unsteady flows are analyzed. The rest of the paper is organized as follows. The governing equations of the SPH method and its numerical implementation, the GPUSPH model, are introduced in Section 2. Section 3 presents the physical experiment and the corresponding numerical setup. Section 4 compares the numerical results with the laboratory measurements including the free surface evolution, hydrodynamic force, and velocity. Then Section 5 discusses the blockage effects of different shapes of bridge piers, the influence of pier shape on wave impact, and the bed shear stress distribution around a bridge pier under the attack of a tsunami bore. Finally, the conclusions are in Section 6.

2. Numerical model

2.1. Governing equations of the SPH method

In an SPH model, the computation domain is discretized into a set of particles, which possess material properties, such as mass, velocity, density, and pressure. Under the framework of the large eddy simulation, the mass and momentum equations of particles are derived from the Navier–Stokes equations by using a spatial filter and written as follows:

$$\frac{D\rho}{Dt} = -\rho \nabla \cdot \mathbf{u} \quad (1)$$

$$\frac{D\mathbf{u}}{Dt} = -\frac{\nabla P}{\rho} + \mathbf{g} + \nu_0 \nabla^2 \mathbf{u} + \frac{1}{\rho} \nabla \cdot \boldsymbol{\tau} \quad (2)$$

where t is time; ρ is fluid density; \mathbf{u} is particle velocity; P is pressure; \mathbf{g} is the gravitational acceleration; ν_0 is the laminar kinematic viscosity; and $\boldsymbol{\tau}$ is turbulence stress tensor, which is approximated by the sub-particle scale (SPS) model (see, e.g., Dalrymple and Rogers, 2006):

$$\tau_{m,n} = \rho \nu_t \left(\frac{\partial u_m}{\partial x_n} + \frac{\partial u_n}{\partial x_m} - \frac{2}{3} \delta_{m,n} \sum_{k=1}^3 \frac{\partial u_k}{\partial x_k} \right) - \frac{2}{3} \rho C_I \Delta^2 \delta_{m,n} \|S\|^2 \quad (3)$$

where the constant parameter $C_I = 0.0066$; Δ is the initial particle spacing $\delta_{m,n}$, is the Kronecker delta; and the shear stress component directions m and n follow the Einstein notation. The turbulent viscosity is determined by the Smagorinsky turbulent model (Smagorinsky, 1963):

$$\nu_t = (C_{smag} \Delta)^2 \|S\| \quad (4)$$

where C_{smag} is the Smagorinsky constant, which is determined by calibration in this study. The strain rate tensor is $S_{m,n} = \frac{1}{2} \left(\frac{\partial u_m}{\partial x_n} + \frac{\partial u_n}{\partial x_m} \right)$ and its norm is defined by $\|S\| = (2S_{m,n}S_{m,n})^{1/2}$, which is further expanded as

$$\|S\|^2 = 2 \sum_{m=1}^3 \left(\frac{\partial u_m}{\partial x_m} \right)^2 + \sum_{m=1, n \neq m}^3 \left(\frac{\partial u_m}{\partial x_n} + \frac{\partial u_n}{\partial x_m} \right)^2 \quad (5)$$

In this study, the fluid is assumed to be weakly compressible, then the pressure can be directly computed by using the equation of state (Monaghan, 1992) as follows

$$P = \beta \left[\left(\frac{\rho}{\rho_0} \right)^\gamma - 1 \right] \quad (6)$$

where ρ_0 is the initial density; γ is chosen to be 7; and the parameter β is calculated by

$$\beta = \frac{\rho_0 C_s^2}{\gamma} \quad (7)$$

where C_s is the speed of sound. The real speed of sound leads to a very small time step, which is not practical for numerical simulation. A good workaround is to set the ratio of $C_s/u_{max} \geq 10$ (where u_{max} is the maximum velocity in the simulation) by adjusting β . Although this practice gives a slight density fluctuation (that is $< 1\%$ as required by Monaghan (1994)), a very important gain is that the governing equations can be solved explicitly; this further allows numerical implementation to utilize the latest parallel computing techniques.

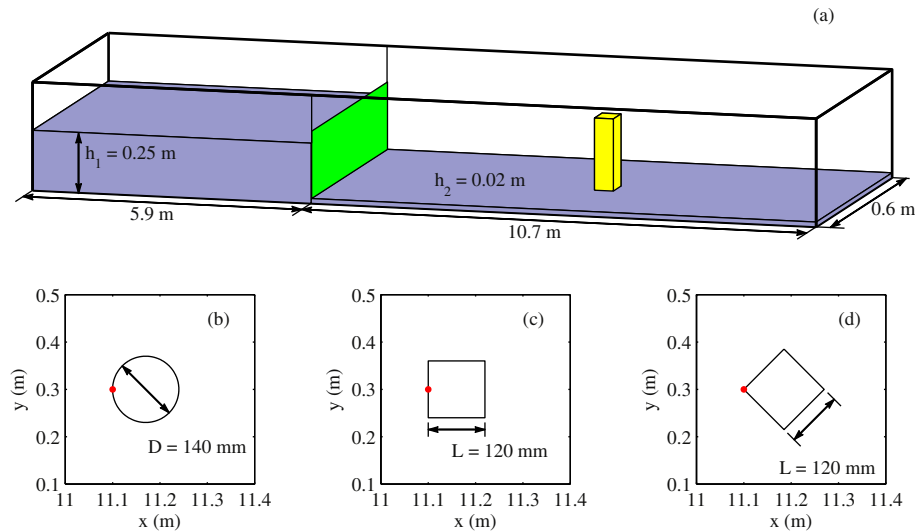


Fig. 1. Definition sketch of the physical experiment of Arnason et al. (2009). (a) Overview of experiment, (b) circular bridge pier, (c) square bridge pier, and (d) diamond bridge pier.

2.2. Numerical implementation: GPUSPH model

Héroult et al. (2010) first implemented the above equations with an explicit second-order time marching scheme using CUDA on NVIDIA GPUs, and created the open-source fluid-dynamics SPH code: GPUSPH¹. They showed that GPUSPH running on a single GPU card achieves one to two orders of speedup when compared with the equivalent CPU code.

Recently, several new features have been integrated into GPUSPH, e.g., supporting digital elevation model topography (Héroult et al., 2011), multi-node and multi-GPU modes (Rustico et al., 2012), surface particles detection (Farahani et al., 2013), floating objects (Bilotta et al., 2014), and homogeneous precision (Héroult et al., 2014). In addition to simulation of violent wave processes, GPUSPH has been recently applied to design wave energy converters (Edge et al., 2014), predict nearshore circulations (Farahani et al., 2013), and reveal the generation mechanisms of coherent structures under broken solitary waves (Farahani and Dalrymple, 2014).

3. Physical experiment and numerical setup

3.1. Laboratory experiment

The experiment of Arnason et al. (2009) was performed in a 16.6 m long, 0.6 m wide, and 0.45 m deep wave tank as shown in Fig. 1(a). A gate separated a thin layer water of depth 0.02 m downstream with a water depth of 0.25 m behind it. The distance between the upstream end-wall and the gate was 5.9 m, representing a reservoir of $5.9 \times 0.6 \times 0.25 \text{ m}^3$ of water. A single bore was generated by lifting the 6.4 mm thick stainless steel gate in 0.2 s or less with the aid of a pneumatic cylinder. A vertical column (i.e., a simplified bridge pier) was placed at 5.2 m downstream of the gate (i.e., $x = 11.1 \text{ m}$ from the upstream end of the tank). To evaluate a tsunami bore impact on different shapes of bridge piers, three configurations are considered in this study. The first pier, referred to as *circular*, is a circular column with the diameter equal to 140 mm as shown in Fig. 1(b). The other two bridge piers are square shaped with a side length equal to 120 mm; the difference is that one, referred to as *square*, has one side facing the incoming bore as shown in Fig. 1(c), and the other one, referred to as *diamond*, has one edge facing the incoming bore as shown in Fig. 1(d). It is worth pointing out that the leading part of the three bridge piers was

exactly placed at $x = 11.1 \text{ m}$ and $y = 0.3 \text{ m}$, which guarantees that all bridge piers, at least in principle, are struck by the same incoming bore.

There are several challenges in terms of numerical simulation of this experiment. First, Arnason et al. (2009) showed that the generated tsunami bore is transient and supercritical with a Froude number about 1.3 in front of the bridge pier ($Fr = \frac{u_2}{\sqrt{gh_2}}$, where u_2 is the incoming bore velocity; h_2 is the incoming bore depth, as indicated in Table 1 and Fig. 2 of Arnason et al. (2009)). Second, with the relatively long distance (i.e., 5.2 m) between the gate and the bridge pier, the correct prediction of the tsunami bore arrival time at the front of the pier is essential to the subsequent hydrodynamic impact. It should be mentioned that Gómez-Gesteira and Dalrymple (2004) simulated a version of this experiment and computed the wave impact on a vertical square column by using the open-source SPH model, SPHysics. The biggest difference with this work is that their experimental domain in the longitudinal direction (i.e., 1.6 m in total) is much shorter than the dimension in the actual experiment. As a result, the bore studied by Gómez-Gesteira and Dalrymple (2004) was not well established, hence transient. On the other hand, the bore generated by Arnason et al. (2009) was well developed and could be considered as a uniform bore, i.e., the classic definition of a bore. Regarding the similar work done by St-Germain et al. (2014), although their experimental dimension is close to that considered in this study, the particle size they used is six to ten times coarser than the size used in this work. As a result, the predicted arrival time and dynamic force of the tsunami bore are influenced, as shown in Fig. 18 of their paper. Furthermore, a coarser particle size is unable to predict a realistic free surface field at the moment of wave impact.

3.2. Numerical model setup

In GPUSPH, the experimental domain is discretized into a collection of particles with a particle size of 0.005 m. As a result, the total number of particles is about 12 million, of which 8 million are fluid particles. The remaining particles are boundary and gate particles. Regarding the boundary condition, although there are several options as reported in literature (see, e.g., Monaghan, 1994; Monaghan and Kos, 1999), the dynamic boundary condition presented by Dalrymple and Knio (2000) and Crespo et al. (2007) is used with 3.7 million boundary particles. This boundary condition establishes several rows of boundary particles, and these dynamic boundary particles share the same equations of continuity and state as the fluid particles placed inside the domain; however, their positions and velocities remain unchanged in time. In the numerical simulation, the bore is generated by lifting the gate in 0.2 s.

¹ The code is freely available at: www.gpusph.org.

In terms of numerical parameters, the SPS viscosity model with the Smagorinsky constant of 0.2 is used by calibration. A fifth-order quintic function of Wendland (1995) is used as the weighting function (kernel) in this study. To ensure that the free surface is smooth and physically acceptable, the particle density is Shepard filtered every 20 steps (Dalrymple and Rogers, 2006). Regarding the speed of sound C_s , it is chosen based on the principle that the ratio C_s/u_{max} should be larger than 10 (Monaghan, 1994). This study first validates the model by considering a test without a bridge pier downstream, and then investigates tests with the bridge piers included (*bridge pier tests*, hereafter).

The numerical simulations were carried out by running GPUSPH on 6 NVIDIA Tesla C2050 GPUs, each of them has a compute capability of 2.0 (NVIDIA, 2014). The numerical model simulates 13 s of the physical experiment, and it requires approximately 90 h of computation for cases with a bridge pier downstream.

4. Results

Prior to applying GPUSPH to simulate a tsunami bore impact on bridge piers, it is first validated by running a test without a bridge pier

in place. Then the free surface time history around different bridge piers is presented. Next, the tsunami bore force on bridge piers is examined. Finally, the velocity field around and in the wake of the circular bridge pier is compared with the experimental data.

4.1. Model validation

For the validation test there is no bridge pier present, but the other test conditions such as water depths upstream and downstream are the same with those used by the bridge pier tests. First, the significance of gate lifting on the generated tsunami bore is investigated, and then the time-series free surface profile at $x = 11.1$ m, which is at the same location of the leading edge of bridge piers, is compared with the experimental data.

In the physical experiment of Arnason et al. (2009), the tsunami bore was generated by lifting the gate out of the 0.45 m tall flume in around 0.2 s. In the numerical model, the initially stationary gate was also removed in 0.2 s; this assumption gives an approximate acceleration of the gate of 22.5 m/s^2 . Fig. 2 shows the comparison of the initial stage of bore generation with the 0.2 s gate lifting operation and that with

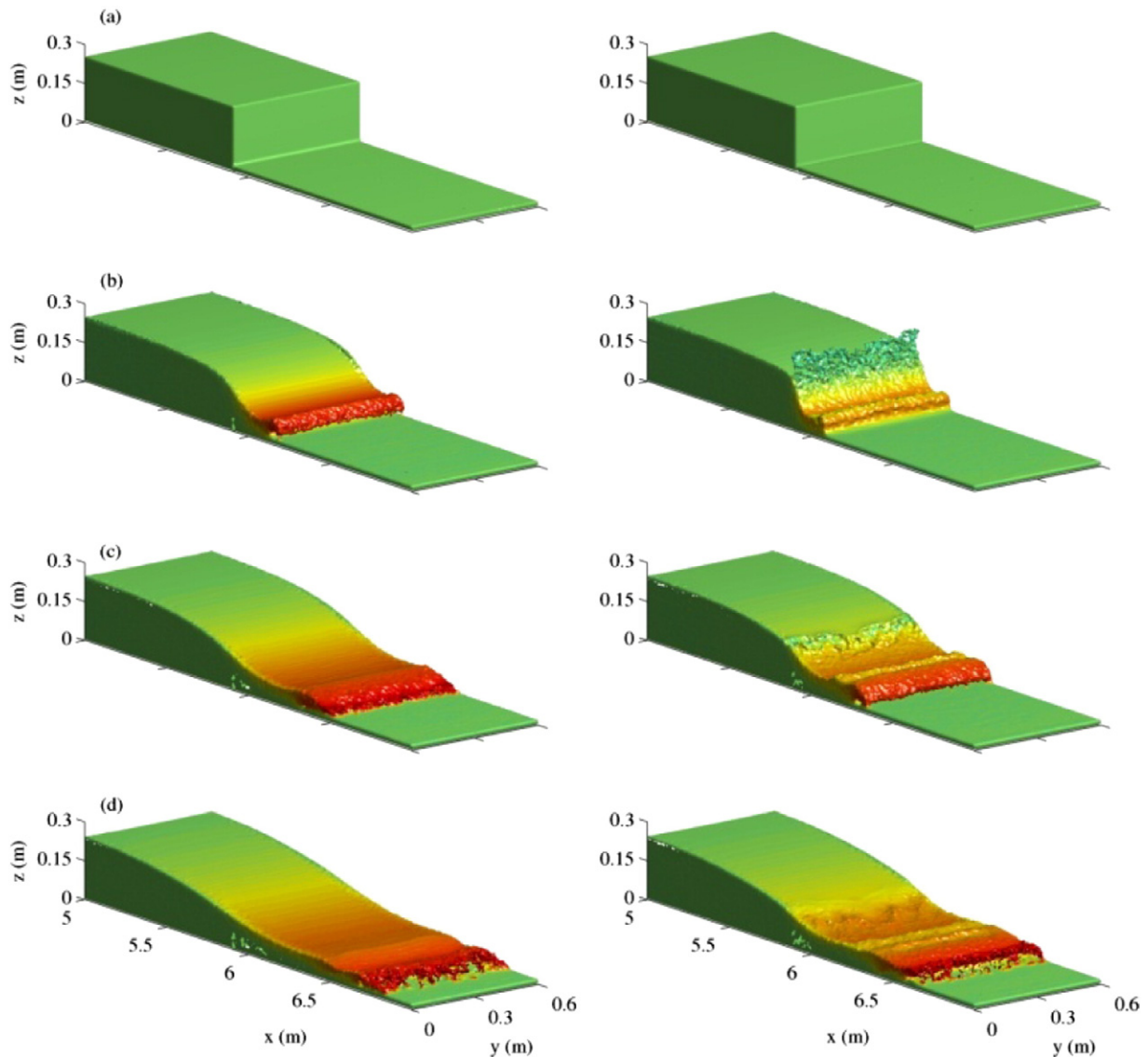


Fig. 2. Comparison of initial stage of a tsunami bore generation with an instantaneous gate removal (left panel) and with a 0.2 s gate lifting (right panel). (a) $t = 0$ s, (b) $t = 0.2$ s, (c) $t = 0.35$ s, and (d) $t = 0.5$ s.

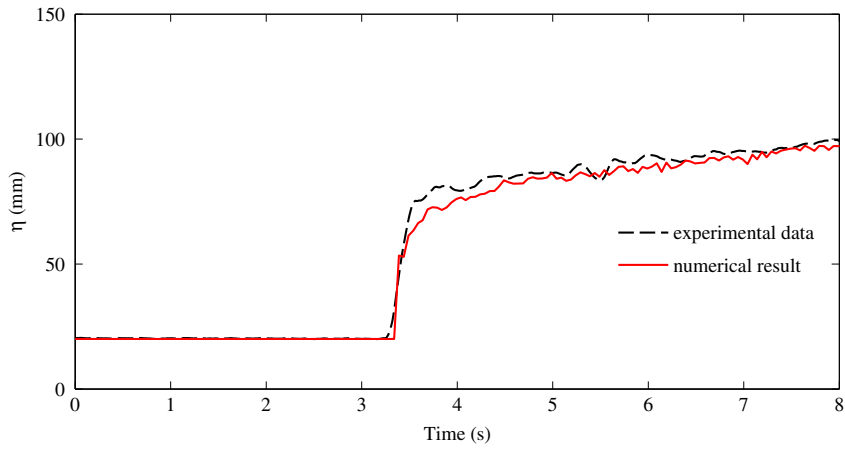


Fig. 3. Comparison of the measured time-series of free surface elevation 5.2 m downstream of the gate (i.e., $x = 11.1$ m) without considering bridge piers of Arnason et al. (2009) with the prediction of GPUSPH.

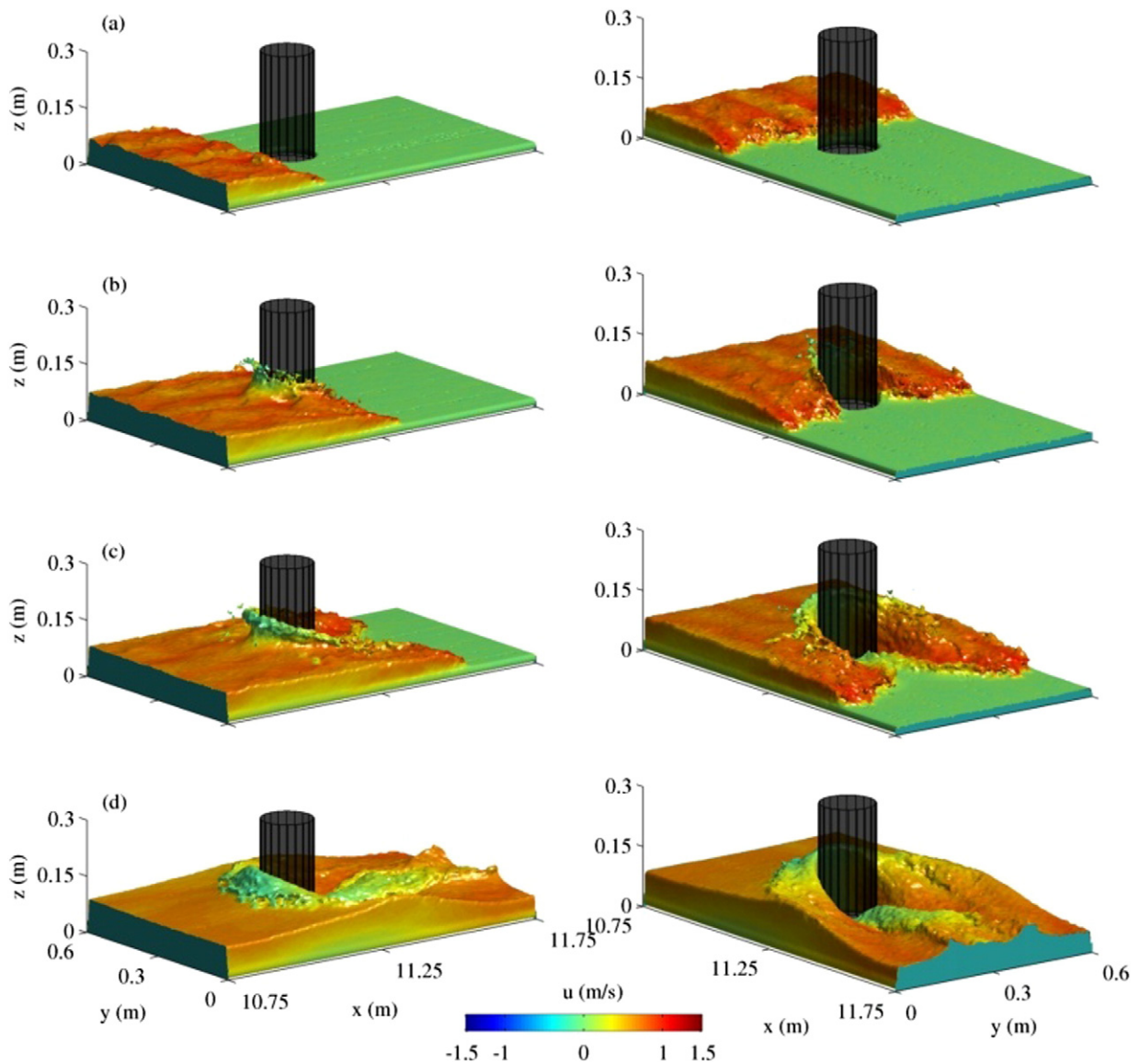


Fig. 4. Snapshots of a tsunami bore impinging on the circular bridge pier with both upstream (left panel) and downstream (right panel) views. (a) $t = 3.3$ s, (b) $t = 3.45$ s, (c) $t = 3.6$ s, and (d) $t = 4.0$ s. The color denotes longitudinal velocity.

an instantaneous gate removal. Before the gate is lifted or removed, both cases have the same initial free surface profile as indicated in Fig. 2(a). At $t = 0.2$ s, there is a large difference between these two cases. For the case with the instantaneous gate removal, there is a surge formed at the wavefront, and it is plunging over the tailwater (the left panel of Fig. 2(b)). For the other case with the accelerating gate, water particles near the gate are dragged into the air due to the gate motion (the right panel of Fig. 2(b)). Although there is still a surge formed, it hasn't started to plunge into the water. At $t = 0.35$ s, the difference is more obvious as shown in Fig. 2(c). The case with the instantaneous gate removal has a relatively smooth bore front, and it has already arrived at $x = 6.5$ m (recall that the gate position is at $x = 5.9$ m). For the other case, the generated tsunami bore is very turbulent, and it is just plunging into the shallow water. Furthermore, it only reaches a point around $x = 6.3$ m, which indicates that there is a 0.2 m lag between these two operations even after 0.35 s of dam-breaking. The difference can be further observed in the instantaneous free surface profile at $t = 0.5$ s, as shown in Fig. 2(d). Overall, the above comparison shows that gate lifting, even if it is very short, still has a great impact on the generated bore shape.

By using the Method of Characteristics, Arnason et al. (2009) predicted that the tsunami bore velocity is between 1.24 and 1.58 m/s in the validation test. For the bridge pier tests presented in the following sections, a larger maximum velocity is expected due to bore-pier impact and flow constriction around the pier; an initial numerical test by GPUSPH showed that the maximum velocity was within the range of 3 m/s. Therefore, following the rule of $C_s/u_{max} \geq 10$ presented by Monaghan (1994), a $C_s = 30$ m/s is used by GPUSPH. The time-series free surface profile at $x = 11.1$ m in the validation test (i.e., without a bridge pier downstream) is shown in Fig. 3. It is seen that the arrival time of the tsunami bore predicted by the numerical model is almost the same as the measurement. Furthermore, numerical simulation also captures the sharp free surface rise similar to the experimental data. However, there is an under-prediction of free surface elevation about 2 particle sizes (i.e., 10 mm) after the bore arrives at the gage shortly (around $t = 3.8$ s). Due to the release of a large amount of water from the impoundment, the rise in elevation continues for several seconds. Considering that the unit of free surface elevation plotted in Fig. 3 is mm, the numerical simulation actually matches very well with the experimental data.

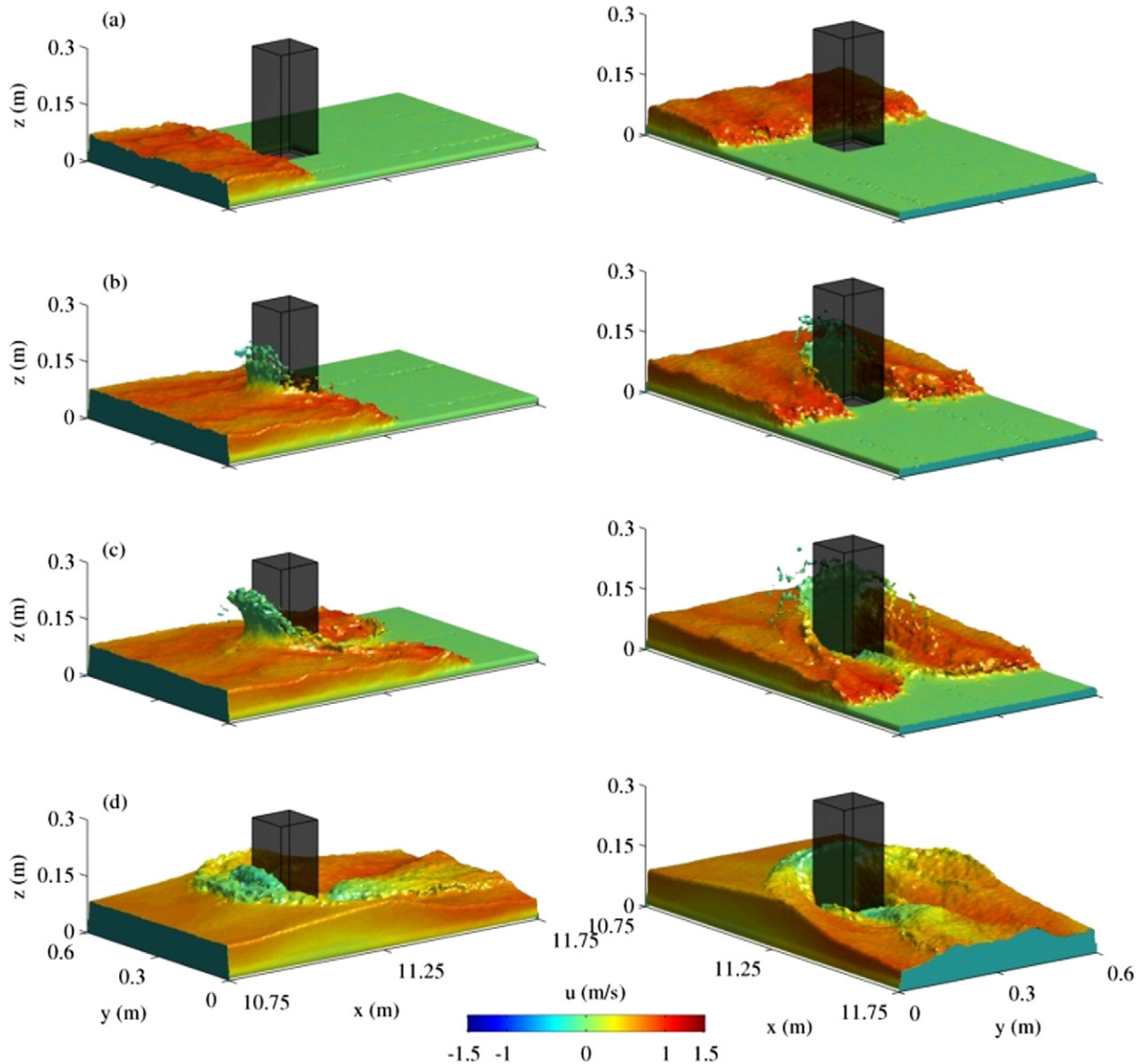


Fig. 5. Snapshots of a tsunami bore impinging on the square bridge pier with both upstream (left panel) and downstream (right panel) views. (a) $t = 3.3$ s, (b) $t = 3.45$ s, (c) $t = 3.6$ s, and (d) $t = 4.0$ s. The color denotes longitudinal velocity.

4.2. Free surface evolution

The free surface evolution and wave–structure interaction of a tsunami bore impact on the circular bridge pier is shown in Fig. 4. The tsunami bore arrives at the front of the bridge pier around $t = 3.3$ s, and it is seen that the bore is unsteady and turbulent as the wavefront is not smooth from the downstream view of Fig. 4(a). As the tsunami bore strikes the pier, a run-up is formed within 0.15 s (Fig. 4(b)). As the tsunami bore continues to travel downstream, it wraps around the pier; meanwhile, the upstream water depth is still increasing at $t = 3.6$ s (Fig. 4(c)). After the water rises to a certain height, the run-up jet falls back due to gravity. The two branches of the tsunami bore pass the pier and collide at the lee side, creating the so-called rooster tail that oscillates around the centerline downstream; see the free surface field at $t = 4.0$ s in Fig. 4(d). The water depth in front of the pier continues to rise at a slowly increasing rate for several seconds augmented by the pier blockage. As a result, the supercritical flow in front of the bridge pier gradually transitions into a subcritical flow. Then the wave created by the flow blockage propagates upstream.

The tsunami bore impact on the square bridge pier is presented in Fig. 5. The selected four time intervals are the same with those used

by the circular bridge pier. At $t = 3.3$ s, the tsunami bore arrives at the front of the square bridge pier, the bore front is similar to that observed in the circular case (Fig. 5(a)). As the square bridge pier has one side facing the incoming bore, the run-up observed in this case is much higher than that observed for the circular bridge pier; see the free surface profile at $t = 3.45$ s in Fig. 5(b). As time advances, the free surface elevation upstream of the pier also rises further. The wave run-up formed by the collision of the bore on the front face of bridge pier continues to increase. Eventually, the run-up falls backward at $t = 3.6$ s, as shown in Fig. 5(c). As the tsunami bore passes the bridge pier, an unsteady rooster tail also forms at the lee side of the pier; see the free surface profile at $t = 4.0$ s in Fig. 5(d).

By comparing the free surface evolution of the tsunami bore impact on the circular bridge pier with that on the square bridge pier, it is clearly seen that there is a strong influence of bridge pier shape on the dynamic interaction between a tsunami bore and a bridge pier. Next, the free surface evolution for a diamond bridge pier is presented in Fig. 6. The instantaneous profile of a tsunami bore at $t = 3.3$ s is similar to those observed in the above two cases (Fig. 6(a)). However, as the tsunami bore is split by the pier edge, the bore run-up on the front of the pier is small, and a bow wave is formed at $t = 3.45$ s, see Fig. 6(b).

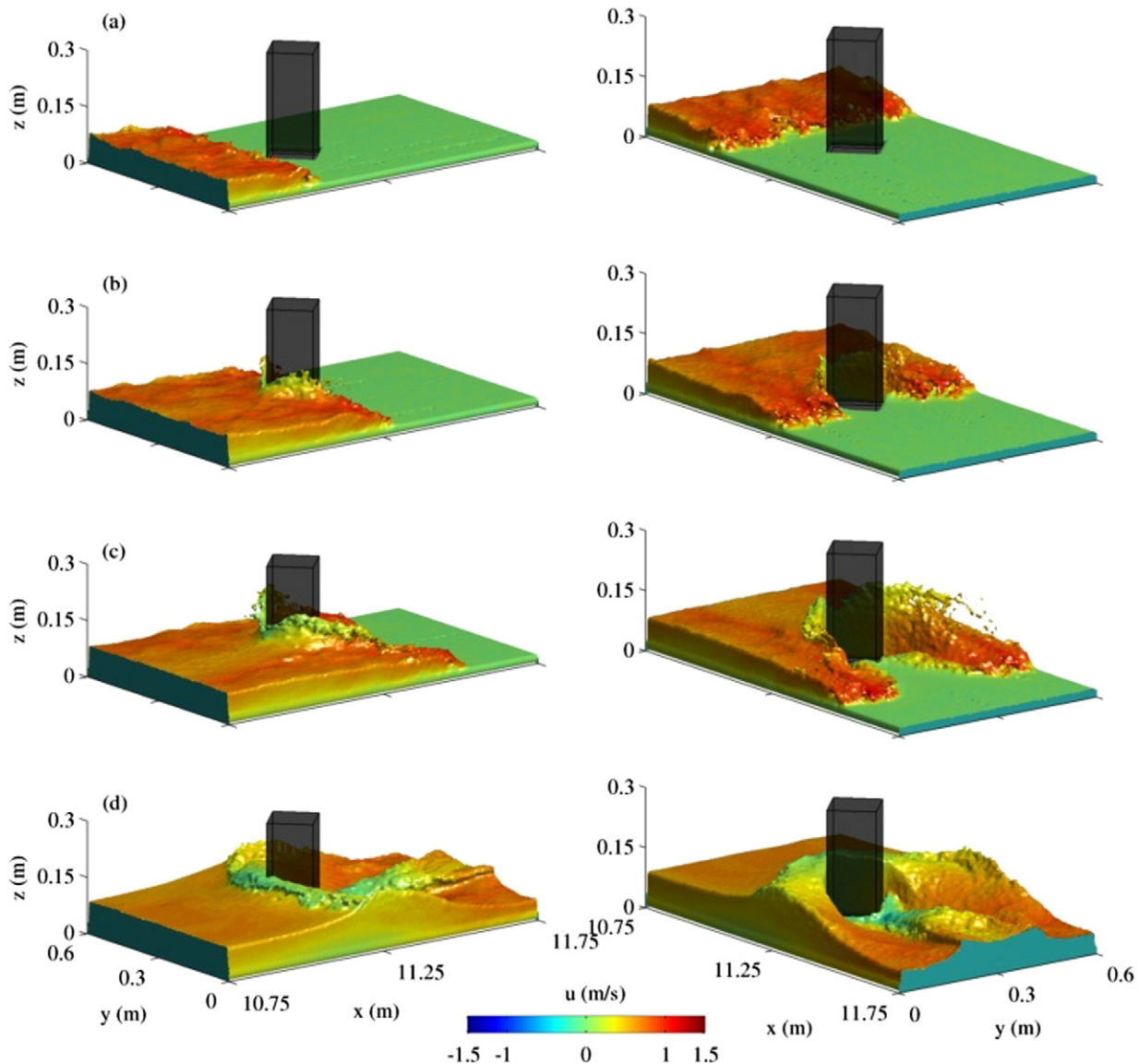


Fig. 6. Snapshots of a tsunami bore impinging on the diamond bridge pier with both upstream (left panel) and downstream (right panel) views. (a) $t = 3.3$ s, (b) $t = 3.45$ s, (c) $t = 3.6$ s, and (d) $t = 4.0$ s. The color denotes longitudinal velocity.

The bow waves in front of the two sidewalls are not very large at $t = 3.6$ s, as shown in Fig. 6(c). The two branches of the bore meet at the lee side of the pier and a transient rooster tail is also formed. As the cross-section width of the diamond bridge pier is larger than that of the square bridge pier, the gaps between the diamond bridge pier and the sidewalls are smaller than those associated with the square bridge pier. As a result, the flow blockage effect due to the diamond pier is more prominent than that due to the square pier, see Fig. 6(d). Overall the dynamic interaction between a tsunami bore and a bridge pier is less violent if there is a clear flow separation point in front of the bridge pier.

Finally, a quantitative comparison between the predicted and the measured wave impingements in front of bridge piers is shown in Fig. 7. One second results of the instantaneous free surface profile along the centerline ($y = 0.3$ m) at the upstream side of bridge pier ($x = 10.8$ m–11.1 m) are presented. The free surface profile in the experiment was obtained by a high-speed video camera. The x coordinate indicates the measurement section with the origin at $x = 11.1$ m; the t coordinate shows the elapsed time with the origin at the point of gate lifting; and the z coordinate shows the free surface elevation with the origin at the bottom. It is seen that the predicted arrival time for all three numerical cases matches well with those in the experiments. For the first bore impact, there are under-predictions by GPUSPH for the circular and square bridge piers (see Fig. 7(a) and (b)). This might be the result of the particle resolution not being fine enough to capture some small breaking events (although the model particle size 0.005 m is already very small), and also there was an under-prediction of the peak incoming tsunami bore profile when comparing with the one in the

physical experiment as mentioned earlier in Section 4.1. However, the free surface profile in front of the diamond bridge pier agrees well with the experimental data, see Fig. 7(c). This is due to the fact that the first impact is less violent (no splash-up) than those observed in the other two cases, as explained earlier.

4.3. Hydrodynamic force

The tsunami loadings on coastal structures can be categorized into several components, such as hydrostatic force, hydrodynamic force, and surge force (e.g., Yeh et al., 2005). In this study, the major tsunami bore force exerted on a bridge pier is the hydrodynamic force caused by the frontal impact and drag along the sides. In an SPH model, the external force exerted by neighboring particles on a particle is part of the numerical solution. As the bridge piers are represented by the dynamic boundary particles in this study, the computed hydrodynamic force on the pier is the summation of external forces exerted by fluid particles on those boundary particles. The time-series of computed and measured hydrodynamic forces on bridge piers is shown in Fig. 8. For all three configurations, the initial loading of a tsunami bore on the pier is accurately captured, as is the sharp rise of force within the first 0.3 s of the impact. There is a minor discrepancy between the measurement and the numerical prediction observed in the later stage. The difference is attributed to: (1), the difficulty in reproducing every detail of a specific experiment involving violent motions; and (2), there is an under-prediction of free surface profile as already seen in Fig. 7. For the square bridge pier case, there is a slight peak force around $t = 3.7$ s in the measurement due to the run-up observed in Fig. 5(b) and (c), which has also been captured by GPUSPH. The agreement between the measurement and the simulation is quantitatively evaluated by the coefficient of variation of the root-mean-square error (RMSE). First of all, RMSE is defined as

$$RMSE = \sqrt{\frac{\sum_{k=1}^m (F_{e,k} - F_{s,k})^2}{m}} \quad (8)$$

where k is the sample index; m is the total number of sample force in the measurement and the simulation; F_e and F_s are the measured and the simulated forces, respectively. The 13 s force profile as presented in Fig. 8 is considered and the sample interval is 0.05 s. Furthermore, the coefficient of variation of RMSE is defined by

$$CV(RMSE) = \frac{RMSE}{\bar{F}_e} \quad (9)$$

where \bar{F}_e is the mean of the measured force.

It is found that the coefficient of variation values are 12%, 11%, and 6% for the circular, the square, and the diamond cases, respectively. This indicates that the overall agreement obtained in the diamond bridge pier is better than those obtained in the other two cases. In general, GPUSPH predicts the tsunami hydrodynamic force on different configurations of piers reasonably well. It is worth pointing out that the physical experiment of Arnason et al. (2009) was conducted in a flume with a width of 0.6 m and three types of vertical columns also have different widths. Therefore, the hydrodynamic force presented in Fig. 8 not only includes the drag along the pier, but also the blockage effect of the bridge pier. Further discussion on force separation will be made in Section 5.1.

4.4. Velocity field

In the experiment of Arnason et al. (2009), velocity measurements for the circular bridge pier have been collected in two ways. The first one measured the velocity at fixed points by the Laser Doppler velocimeter (LDV), and the other method measured the velocity field by the particle image velocimeter (PIV).

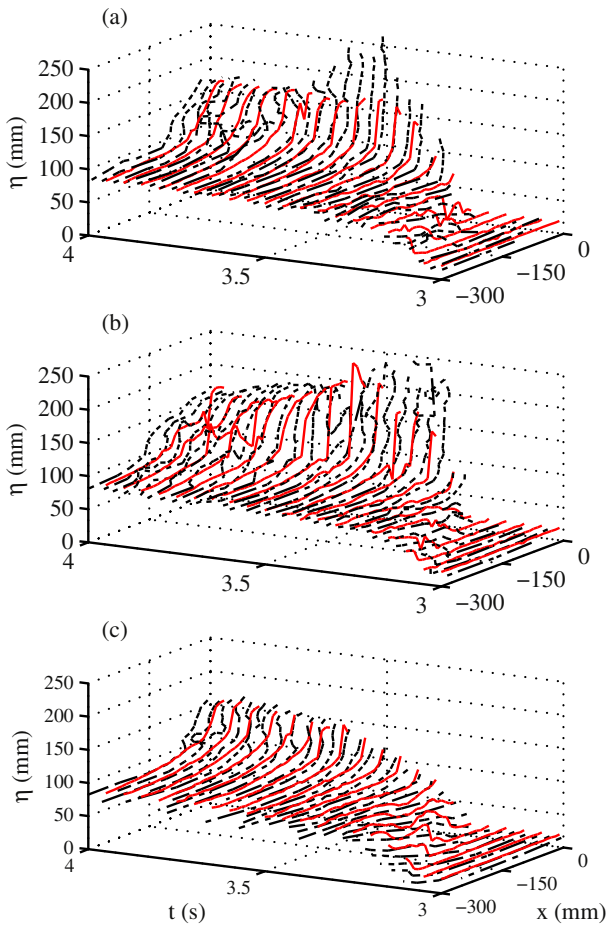


Fig. 7. Comparison of free surface profiles during wave impingement on bridge piers. (a) Circular bridge pier, (b) square bridge pier, and (c) diamond bridge pier. Experimental data of Arnason et al. (2009) (dashed lines), numerical result (solid lines).

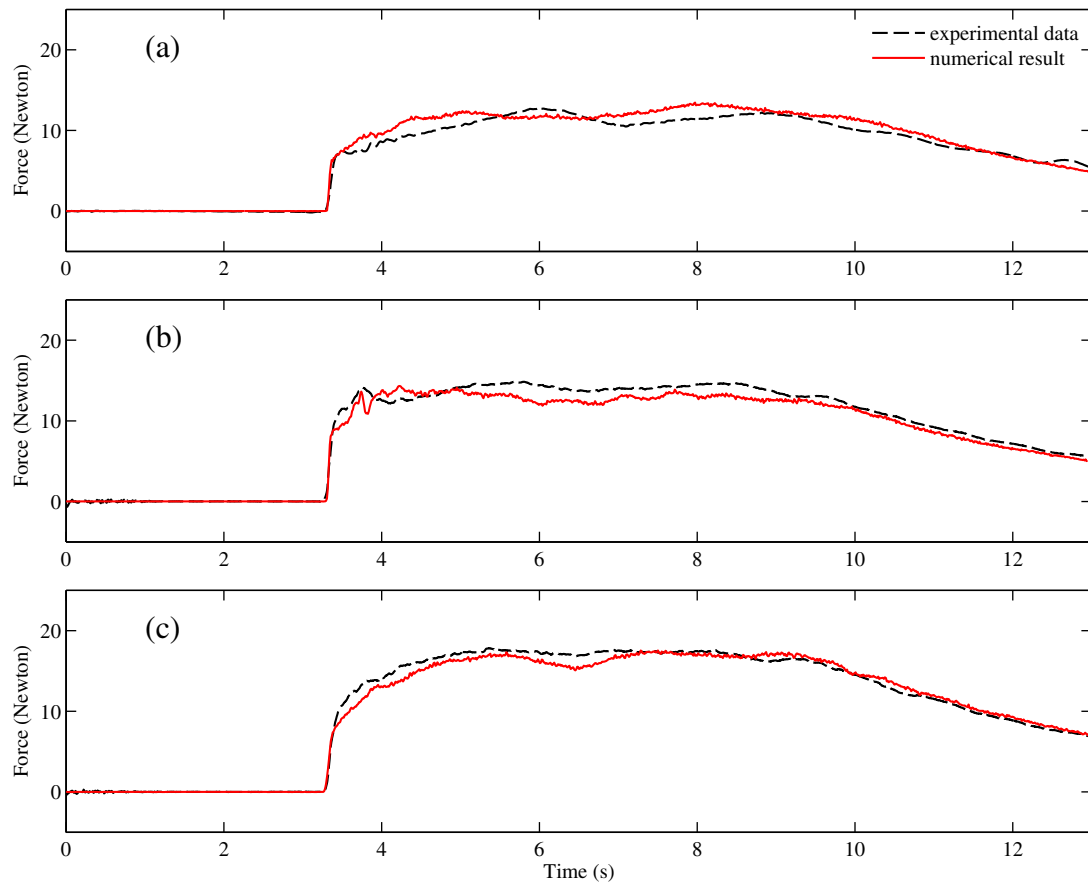


Fig. 8. Comparison of time-series of hydrodynamic forces on bridge piers. (a) Circular bridge pier, (b) square bridge pier, and (c) diamond bridge pier. Experimental data is from Amason et al. (2009).

For the LDV measurement, this study considers four measurement points that are in the wake of the circular bridge pier as indicated in Fig. 9. The first two points placed at section $x = 11.45$ m are closer to the pier. One point is just at the centerline, and the other is placed near the northern side of the flume. Furthermore, each of the points has LDV measurements at two levels $z = 15$ mm and 35 mm. The other two points are located at section $x = 11.57$ m, and they have the same setups as points placed at section $x = 11.45$ m. Comparison of time-series of velocity measurement is shown in Fig. 10. For the first point, the tsunami bore arrival time is correctly captured, and the longitudinal velocity at both levels match with the experimental data reasonably well. For the

transverse velocity, it is seen that both measurement and numerical simulation are small and random; this is due to the fact that the measurements are made in the wake at the rooster trail oscillation zone. For the second point, there is a very good agreement for both the longitudinal and transverse velocities comparison at two levels. It is seen that the point that is located off the center of the flume has a negative transverse velocity toward the center line. As the incoming flow approaches the bridge pier, its direction is slightly changed due to the flow blockage. Because of the narrow flume, the oblique flow quickly reaches the sidewalls (e.g., the northern sidewall), and then it is reflected back into the flume, resulting in a negative velocity. For the other two points at section $x =$

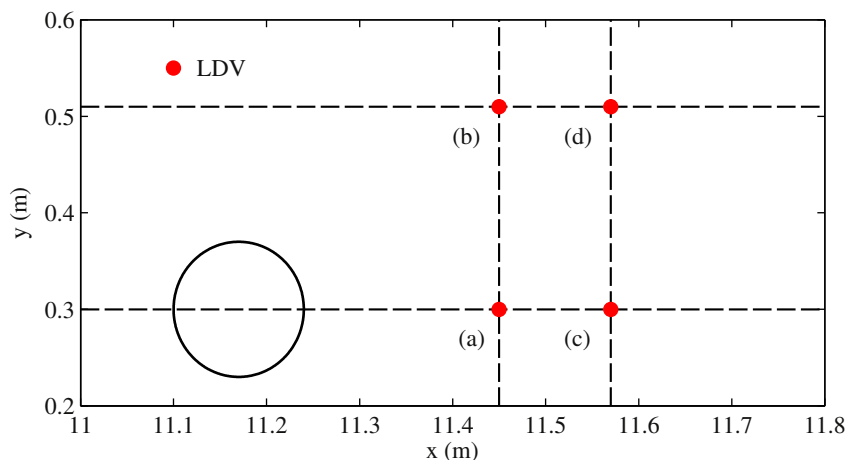


Fig. 9. Location of four LDV measurement points in the wake of the circular bridge pier in the experiment of Amason et al. (2009).

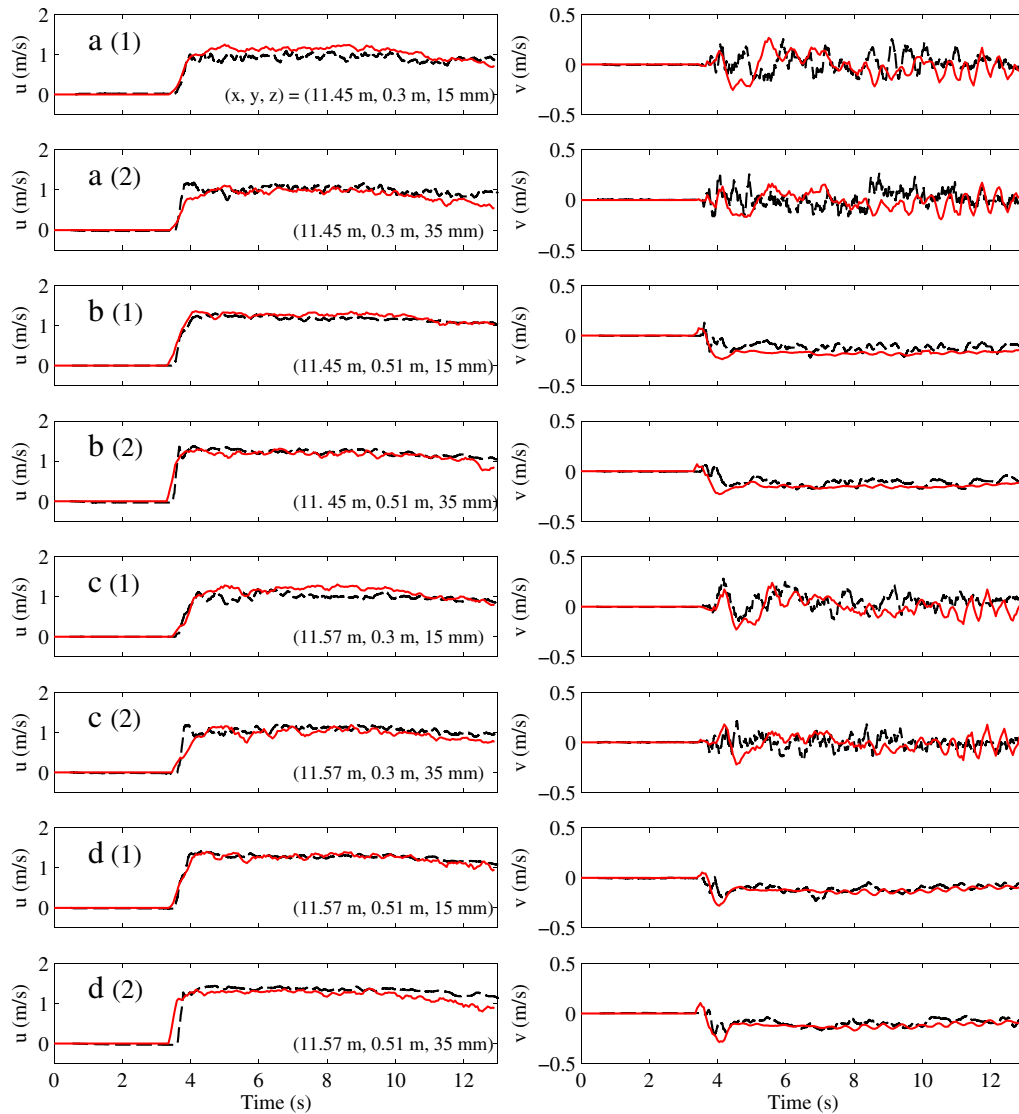


Fig. 10. Comparison of time-series of longitudinal velocity (left panel) and transverse velocity (right panel) at four LDV measurement points in the wake of the circular bridge pier with two levels ($z = 15$ mm and 35 mm). Locations of LDV measurement points are indicated in Fig. 9, experimental data of Amason et al. (2009) (dashed lines), and numerical results (solid lines).

11.57 m, the observations presented above are in general applicable to them.

The LDV result comparison presented above shows that GPUSPH is able to simulate the velocity at scattered points (with different elevations) in the wake of bridge pier very well. Next, numerical result of velocity field around and in the wake of the bridge pier is compared with the PIV measurements. Fig. 11 shows the PIV results at two instants, $t = 4$ s and 7 s; and similar to the LDV results, two levels $z = 15$ mm and 35 mm are compared. The instantaneous free surface profile at $t = 4$ s has been shown in Fig. 4(d), and the hydrodynamic force at $t = 4$ s is continuing to increase as indicated in Fig. 8. Therefore, at this instant the tsunami bore is just passing the pier; hence the flow is highly transient. The upstream comparison between numerical results and the measurements agrees well for both levels. A discrepancy appears near the pier at $z = 15$ mm. It is seen that the numerical prediction shows a stronger deflection from the pier than that measured in the experiment. After the bore passes the pier, the flow confined by the sidewall is reflected into the flume. In the upper part of the wake, numerical simulation matches well with the measured velocity in terms of velocity direction and magnitude. As the flow field is random in nature in the wake of bridge pier, it is expected that numerical simulation cannot match the individual velocity direction exactly, in particular,

in the rooster trail oscillation zone. However, it is seen that the overall magnitude of velocity field is predicted reasonably well. At $t = 7$ s, the water upstream of the bridge pier already started to retreat. As a result, the instantaneous velocity upstream at this time is smaller than that at $t = 4$ s for both levels, as shown in both numerical simulation and the measurement. For the velocity field between the bridge pier and the sidewall, the velocity direction is nearly parallel the sidewall, which indicates the reduction of flux in the incoming bore. Finally, the agreement for the velocity field in the wake is similar to that at $t = 4$ s. By comparing the velocity fields upstream and downstream, it is seen that velocity is relatively smaller upstream due to the flow blockage, but after the flow has passed the bridge pier, its magnitude can be accelerated up to 50% (e.g., from less than 1 m/s to 1.5 m/s as predicted at $t = 4$ s, and $z = 15$ mm). This shows that a tsunami bore may cause more damage downstream in terms of structure failures and river bed erosion for a narrow and confined channel.

5. Discussions

In the previous section, the dynamic interaction between a tsunami bore and bridge piers with different configurations has been investigated.

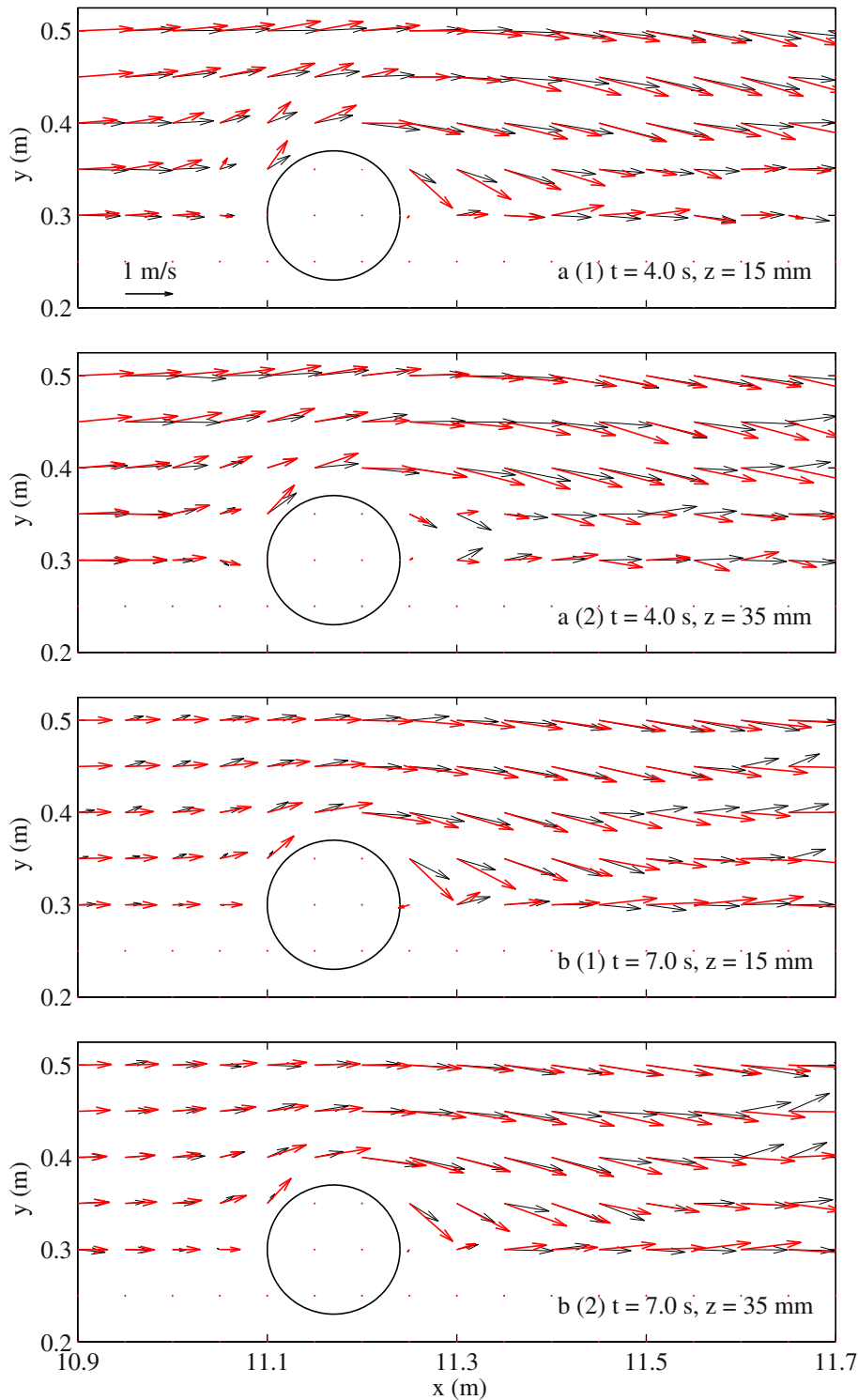


Fig. 11. Comparison of instantaneous velocity field around the circular bridge pier at (a) $t = 4$ s and (b) $t = 7$ s at two levels ($z = 15$ mm and 35 mm). PIV measurements of Arnason et al. (2009) (thin vectors), and numerical results (thick vectors).

The free surface evolution, hydrodynamic force, and velocity field around the circular pier have been compared with laboratory measurements. With the good agreement between the GPUSPH prediction and the measurement in mind, this section further applies GPUSPH to differentiate the hydrodynamic force due to the blockage effect from that caused by the drag effect, explore the details of wave impact on structures, and evaluate the bed shear stress around a bridge pier under a strong tsunami bore.

5.1. Hydrodynamic force: drag effect vs. blockage effect

As pointed out in Section 3, the physical experiment of Arnason et al. (2009) was conducted in a relatively narrow flume with a width of 0.6 m. Due to the sudden release of a large amount of water, the flow was constricted when passing the bridge piers, creating a blockage bow wave in front of bridge piers, as already presented in Sections 4.2,

Table 1

Hydrodynamic force due to blockage effect F_b in terms of dimensionless width (D/W) with $W = 0.6$ m at $t = 12$ s.

| | D (mm) | D/W | F_b (N) |
|----------|----------|-------|-----------|
| Square | 120 | 0.2 | 1.76 |
| Circular | 140 | 0.23 | 1.97 |
| Diamond | 170 | 0.28 | 2.74 |

and 4.4. Considering the above experimental condition, there are two major factors that influence the hydrodynamic force presented in Section 4.3. One is the total drag force on the pier, which is related to the size and the shape of the pier. The other is the force due to the blockage effect by the bridge pier, which is a function of the dimensionless cross-section width of the pier (D/W , hereafter). In this section, an attempt is made to differentiate the hydrodynamic force due to the blockage effect from that caused by the drag.

To address this issue, additional numerical simulations were carried out by expanding the flume width and comparing the newly computed hydrodynamic force with the one in the original setup. Two cases with the flume width $W = 0.9$ m (50% wider) and 1.2 m (100% wider) were considered. The horizontal coordinate of bridge piers' leading edge was still placed at $x = 11.1$ m, and the piers were centered in the transverse direction of the flume as before. Fig. 12 shows the comparison of computed hydrodynamic forces on bridge piers as a function of time with different flume widths. The hydrodynamic force corresponding to $W = 0.6$ m is the one presented earlier in Fig. 8. As the tsunami bore interacts with the bridge piers (say, before $t = 6.5$ s), the bore is highly transient and the blockage effect is not fully established. Consequently, there is no consistent force difference observed among three cases until the main tsunami bore passes the pier around $t = 6.5$ s. After this time, the force difference among all three cases with different widths

was observed. In general, the wider the flume, the smaller the computed hydrodynamic force.

Using the force profiles after $t = 6.5$ s, it is seen that the hydrodynamic force of the 0.6 m wide flume is much different from that of the 1.2 m wide flume; but the one with $W = 0.9$ m is very close to the force computed in the 1.2 m wide flume. Therefore, it is assumed that the 1.2 m wide flume is close to a sidewall-free approximation of the experiment of Arnason et al. (2009), and it can be further used to estimate the lower bound of the hydrodynamic force due to the blockage effect.

As an example, Fig. 13 shows the comparison of free surface profile around bridge piers at $t = 9$ s with the flume widths of 0.6 m and 1.2 m. For the original experimental setup, the flow field is unsteady, and the water is accumulated in front of bridge piers. While for the 1.2 m wide flume, the free surface profile is relatively smooth, and the flow blockage effect is very minor. By reexamining Fig. 12, it can be seen that: (1), near the peak force around $t = 8$ s, the ratio of the hydrodynamic force due to the blockage effect to that caused by the drag effect is about 10%–20% depending on the pier shape; (2), when the flow is less transient and close to steady state (say, after $t = 10$ s), it is easier to identify the relationship between the hydrodynamic force and D/W . First of all, for an individual pier shape, it is found that there is a linear relationship between the total hydrodynamic force and D/W , see the result at $t = 12$ s shown in Fig. 14. This finding is consistent with that obtained by the momentum flux approach presented by Fenton (2003), who showed that the change of surface elevations upstream and downstream of the obstacle, is proportional to D/W . The diamond bridge pier experiences the largest hydrodynamic force due to the blockage effect (i.e., the force difference between the hydrodynamic force computed with $W = 0.6$ m and that with $W = 1.2$ m) and the drag effect, and this is owing to the fact that it has the largest D/W , as presented in Table 1.

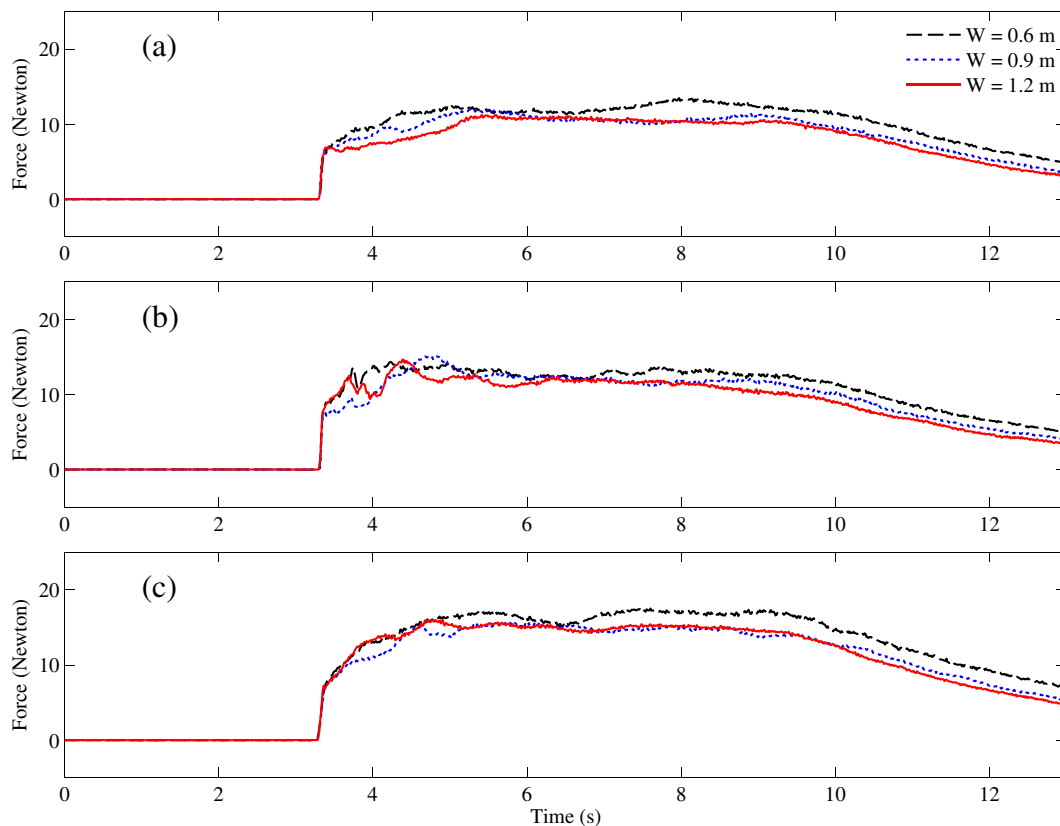


Fig. 12. Simulated hydrodynamic forces on bridge piers by using three different flume widths. (a) Circular bridge pier, (b) square bridge pier, and (c) diamond bridge pier.

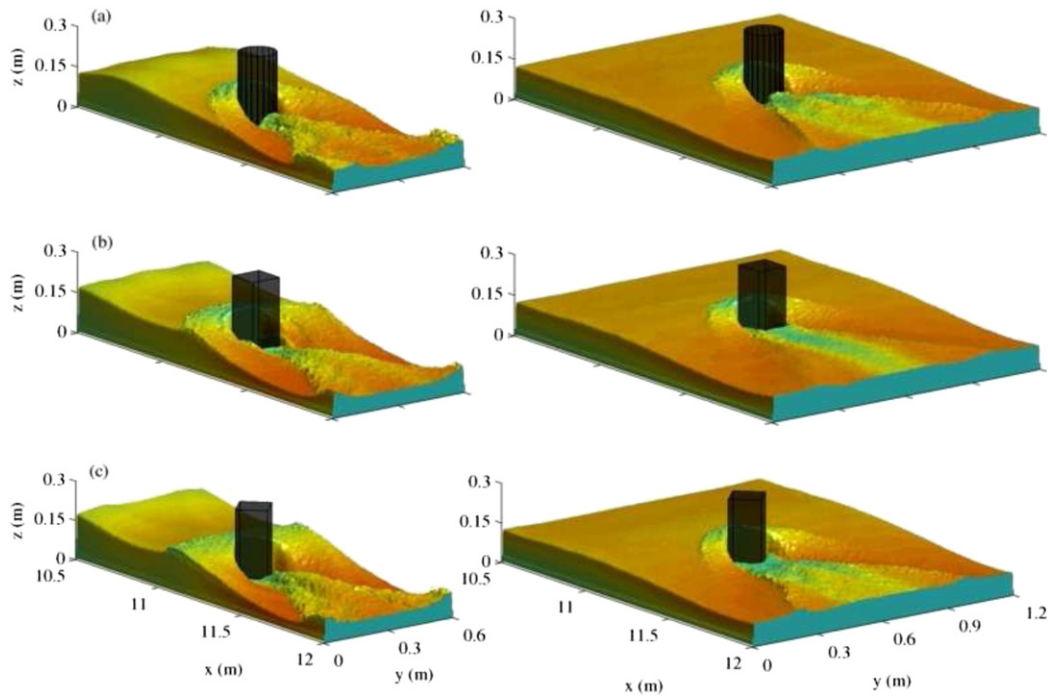


Fig. 13. Comparison of free surface profile around bridge piers at $t = 9$ s with flume width $W = 0.6$ m (left panel) and 1.2 m (right panel). (a) Circular bridge pier, (b) square bridge pier, and (c) diamond bridge pier.

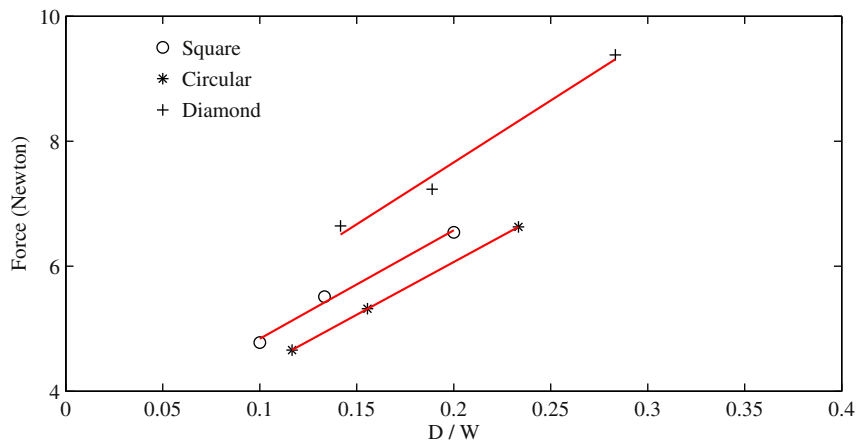


Fig. 14. Hydrodynamic force in terms of dimensionless width (D/W) for three types of piers at $t = 12$ s. Three flume widths, 0.6 , 0.9 , and 1.2 m are considered.

5.2. Wave impingement on structures

Although it has been clearly seen that the tsunami bore attacks the circular bridge pier and the square bridge pier in different ways, the actual wave–structure interaction process is not easily understood. Owing to the Lagrangian nature of an SPH model, individual particle trajectories were tracked during the initial tsunami bore impingement on the circular bridge pier and the square bridge pier. Four particles at

Table 2

Elevation and initial detection time information of four test particles at $(x, y) = (10.6 \text{ m}, 0.3 \text{ m})$.

| No. | Symbol | z (mm) | t (s) |
|-----|--------|----------|---------|
| 1 | ▷ | 30 | 3.2 |
| 2 | * | 40 | 3.25 |
| 3 | ◇ | 55 | 3.3 |
| 4 | ○ | 65 | 3.2 |

$(x, y) = (10.6 \text{ m}, 0.3 \text{ m})$, as indicated in Table 2, are selected with the following considerations: (1), for an individual particle, its elevation and time when it was first detected are approximately the same in both tests; (2), elevations of the selected particles are near the free surface of the tsunami bore, as the wave impingement is the concern of this work; and (3), to avoid the influence of the flow blockage on investigation of wave impingement, the initial detection time of selected particles is earlier than the arrival time of the tsunami bore.

Fig. 15 shows the comparison of particle trajectories in both 3D view and top view. For the circular bridge pier, particles approach the pier in a straight line. Once they reach the front of the pier, all of them rise to a higher elevation due to the flow blockage, and then they fall when passing the pier due to flow expansion. Overall, the flow process is smooth because of the round shape of the circular bridge pier. For the square bridge pier, particles also approach the pier in a straight line. However, it is seen that two particles rise to a very high elevation, corresponding to the run-up observed in Fig. 5. On the other hand, two particles reach the front of the pier and immediately turn toward the bottom. One

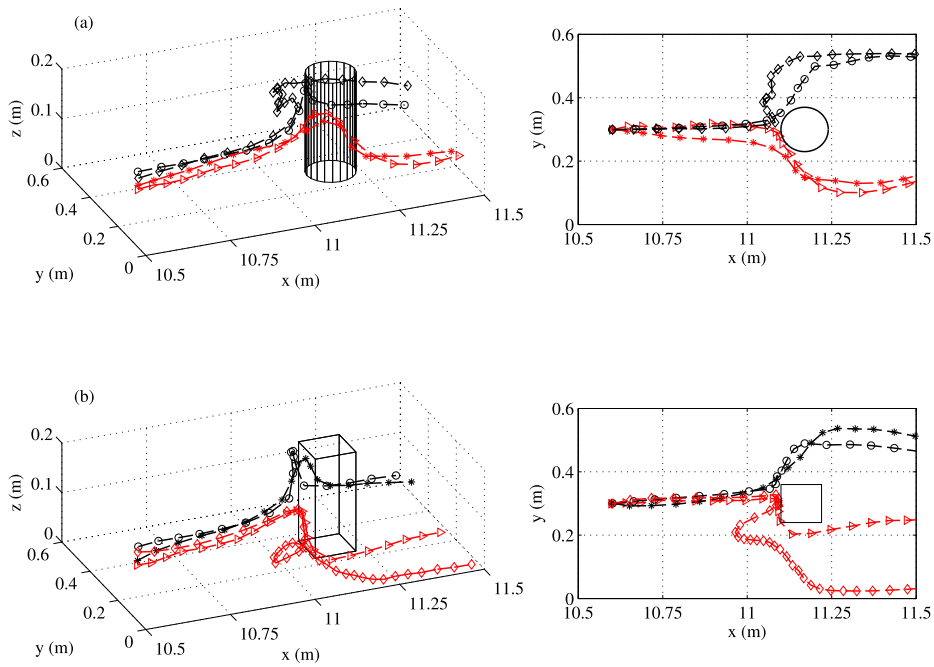


Fig. 15. Particle trajectories around (a) the circular bridge pier, and (b) the square bridge pier. 3D view (left panel), and top view (right panel).

simply passes the pier along its side; the other, however, runs toward upstream more than 0.1 m, and then rises up due to the incoming bore. Eventually it moves downstream along the sidewall. This particle

trajectory in front of the pier actually indicates that there is a turbulent eddy formed by the wave–structure interaction. By comparing the wave impingement processes between the circular bridge pier and the square

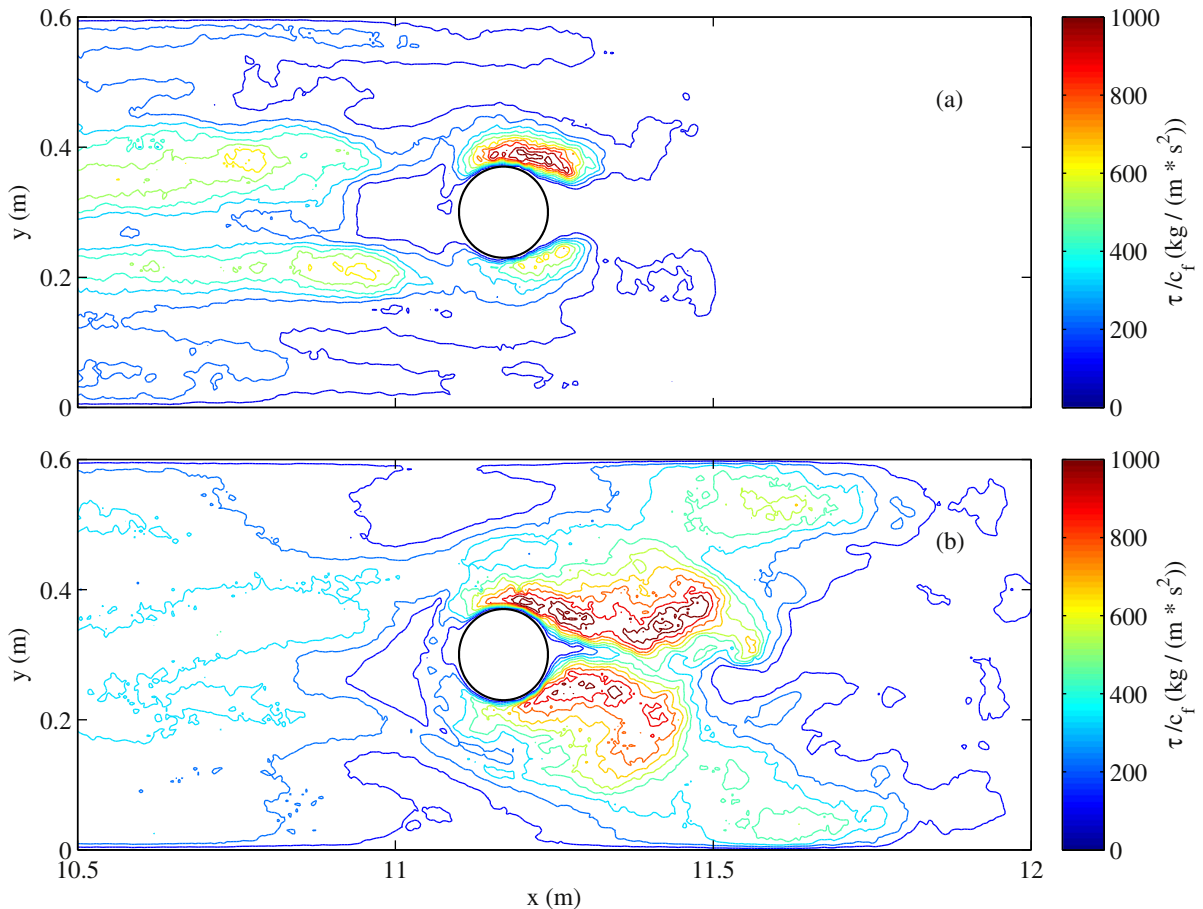


Fig. 16. Instantaneous bed shear stress distributions around the circular bridge pier at (a) $t = 3.6$ s, and (b) $t = 4.0$ s.

bridge pier, it is seen that the first two particles (counting from the bottom) pass the circular bridge pier on its right side. However, in the other test the first and the third particles pass the square pier on its right side. Furthermore, although the elevation and initial detection time are very similar for an individual particle, it still has very different trajectories between two cases. It is also worth pointing out that most of these selected free surface particles travel within the bow wave. As a result, their trajectory pattern is different from a case with no free surface where the particles would pass closer to the pier (see, e.g., the bottom particle in the square bridge pier case indicated with a triangle symbol). Despite the facts that four particles used in this study are unable to represent the whole flow field, and particle motions are also random in nature, the above trajectory test is still very useful to understand the process of wave impingement on different bridge piers and the induced turbulent structure.

5.3. Bed shear stress around a bridge pier under unsteady flows

Significant coastal and estuarine morphology changes induced by the 2011 Great East Japan Tsunami have been observed after the event (Tanaka et al., 2012). Scouring of bridge foundations is identified to be one of bridge failure modes (Kawashima and Buckle, 2013). Tsunami-like solitary wave has been used in physical experiments to investigate tsunami-induced scour around coastal structures and bridge piers (see, e.g., Tonkin et al., 2003; Chen et al., 2013; Yeh and Mason, 2013). It is seen that solitary waves (even a series of solitary waves) have a very limited impact duration on the bridge pier, but a strong tsunami bore as encountered in this study lasts for a

much longer period. Therefore, it is also urgent to study the local scour around a bridge pier under transient flows such as tsunami bores.

To move a sediment particle that is initially at rest on a surface, the bed shear stress τ_b exerted by the fluid must exceed the critical shear stress τ_c of the sediment particle. The critical shear stress τ_c is in general dependent on the properties of the sediment particle such as the grain size. On the other hand, the bed shear stress can be estimated by

$$\tau_b = \rho C_f u_b^2 \quad (10)$$

where C_f is an empirical friction factor; u_b is the velocity of the bottom layer particle that is about 0.01 m above the bed. In this study, as the sediment particle properties (e.g., grain size and cohesiveness) are unknown, the bed shear stress τ_b/C_f around three types of bridge piers is presented and discussed in the following.

As the numerical prediction of the velocity field around the circular bridge pier has been compared with the experimental data in Section 4.4, distributions of the instantaneous bed shear stress at $t = 3.6$ and 4.0 s around the circular bridge pier are discussed in detail in this section. It is recalled that the instantaneous free surface profile at these two instants have been presented in Fig. 4, which shows that the tsunami bore just splashed upon the bridge pier shortly. From the bed shear stress profile in Fig. 16, it is seen that: (1), because of the turbulent and transient flow field, the instantaneous distribution of bed shear stress doesn't show an exact symmetric profile, even though the experimental setup is symmetric in the y direction; (2), due to the stagnation zone in front of the circular bridge pier, the bed shear stress in front of the pier toe is small at these two instants;

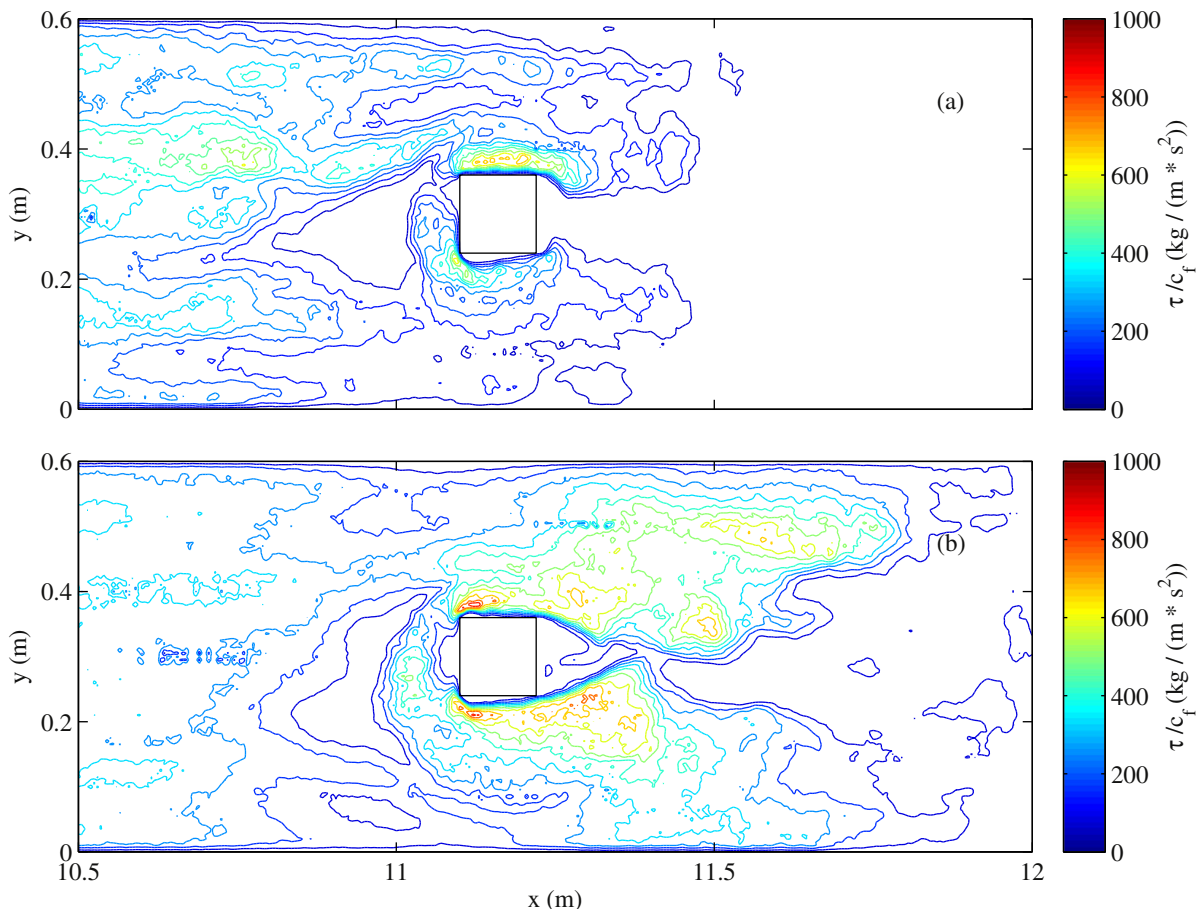


Fig. 17. Instantaneous bed shear stress distributions around the square bridge pier at (a) $t = 3.6$ s, and (b) $t = 4.0$ s.

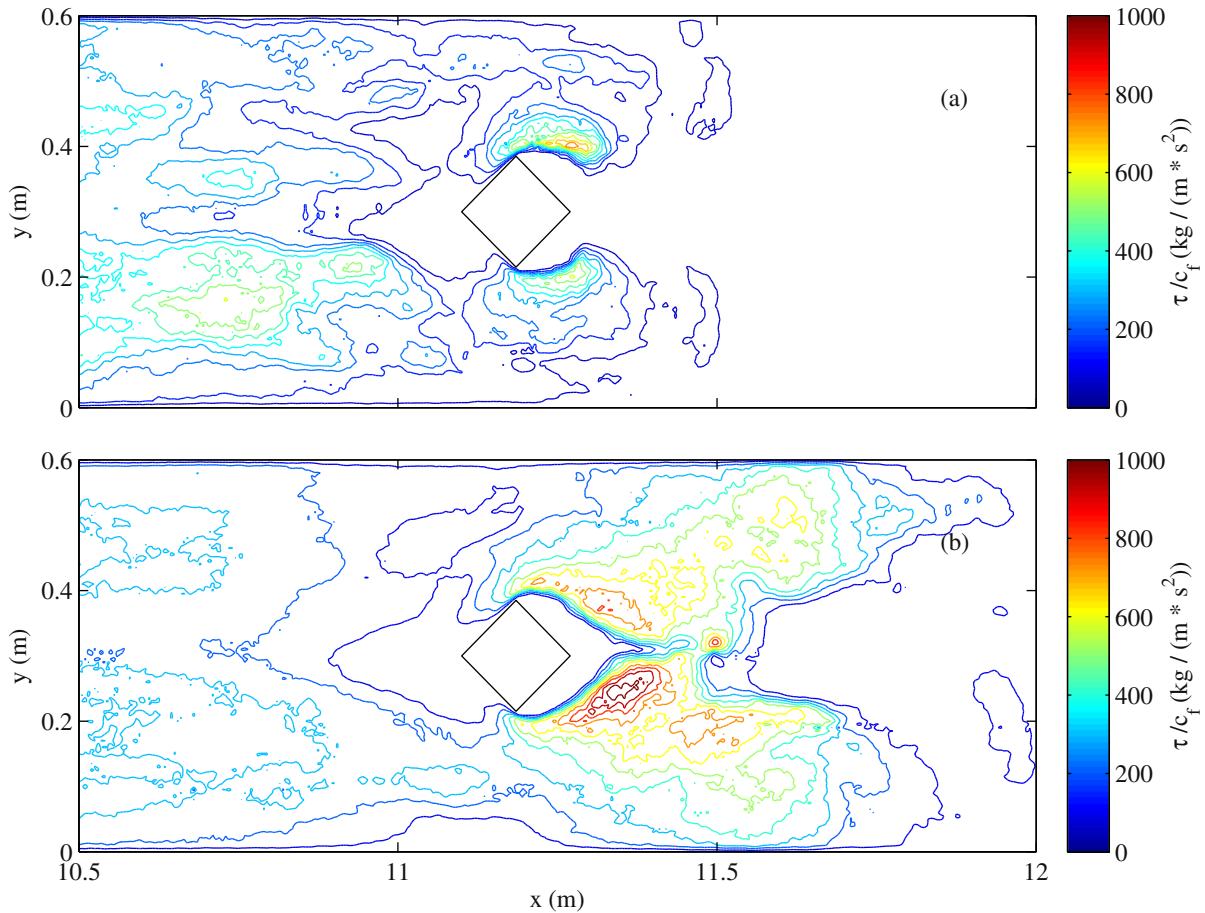


Fig. 18. Instantaneous bed shear stress distributions around the diamond bridge pier at (a) $t = 3.6$ s, and (b) $t = 4.0$ s.

(3), distributions of higher bed shear stress are seen around the (northern and southern) side toes of the bridge pier, they are mainly due to the strong shear drag exerted by high-velocity flows along the pier; and (4), at $t = 4$ s, higher bed shear stress zones are also extended further downstream similar to those observed in the circular bridge pier, as shown in Figs. 17 and 18. In spite of the fact that the above observations are based on the instantaneous bed shear stress at the early stage of tsunami bore attack on the bridge pier, it has been shown in previous sections that the similar flow field to that of $t = 4$ s has been maintained for several seconds due to the steady increment of the incoming flow. As a result, the bed shear stress profile around a bridge pier induced by a real-life tsunami bore might have similar distributions as those presented above.

6. Conclusions

In this study, the dynamic impact of a strong tsunami bore on several simplified bridge piers has been investigated by an SPH model, GPUSPH, which is based on the weakly compressible SPH method and implemented by utilizing the latest GPU parallel computing techniques. The model was first validated by comparing the free surface elevation at a gage that is relatively far from the point where the tsunami bore was

generated. Next, dynamic interactions between a tsunami bore and bridge piers were simulated, and the model showed a good capability to capture the free surface evolution in front of bridge piers. Furthermore, the model was able to accurately compute the tsunami bore hydrodynamic force on different piers. Finally, the velocity field around and in the wake of the circular bridge pier was investigated by GPUSPH, it has been seen that predictions of velocity at scattered points and the overall velocity field agree very well with the measurement obtained by LDV and PIV.

Based on the good numerical results of GPUSPH, the model was applied to differentiate the hydrodynamic force due to the drag effect and that caused by the blockage effect of the pier. It has been seen that the blockage effect is also prominent when compared with the drag force in this work, and the hydrodynamic force is proportional to the dimensionless width of the flume. Furthermore, the wave impingement process on different shapes of bridge piers was investigated, the particle trajectory presented by GPUSPH is helpful to understand the flow structure due to wave impact. Last but not least, the bed shear stress profile around a bridge pier under the attack of a strong tsunami bore was analyzed. This study shows that high bed shear stress zones caused by the tsunami bore are extended downstream of the bridge pier, where the accumulated potential energy is transformed into the kinetic energy due to a sudden flow expansion. It is expected that the wave impingement process and the bed shear stress distribution around a bridge pier in a wider flume would be different from those observed in the narrow flume.

To further the understanding of damage on bridge structures caused by a real-life tsunami disaster, it is seen that several topics should be investigated. This study has simulated the dynamic interaction between a tsunami bore and bridge piers with simple shapes, and bridge piers with

a realistic shape (e.g., Rankine ovoid) should be considered in the future. Furthermore, this study has only addressed the tsunami bore impact on bridge substructure (i.e., bridge pier); it is also important to examine tsunami-induced bore impact on bridge superstructure such as decks and girders.

Acknowledgments

Z.W. and R.A.D. acknowledge the support from the Office of Naval Research, Littoral Geosciences, and Optics Program. R.A.D., A.H., G.B., and E.R. would like to acknowledge the ATHOS Consortium and its member organizations for their contributions to the GPUSPH code. H.Y. was partially supported by the Pacific Earthquake Engineering Research Center and the Edwards endowment. The numerical simulations were carried out at the Graphics Processing Lab Cluster of Johns Hopkins University, which is sponsored by the National Science Foundation grant MRI-0923018.

References

- Arnason, H., Petroff, C., & Yeh, H., 2009. Tsunami bore impingement onto a vertical column. *J. Disaster Res.* 4, 391–403.
- Bilotta, G., Vorobyev, A., Hérault, A., Mayrhofer, A., & Violeau, D., 2014. Modelling real-life flows in hydraulic waterworks with GPUSPH. *Proceedings of the 9th International SPHERIC Workshop*, Paris, France, pp. 335–341.
- Briggs, M.J., Synolakis, C.E., Harkins, G.S., & Green, D.R., 1995. Laboratory experiments of tsunami runup on a circular island. *Tsunamis: 1992–1994*. Springer, pp. 569–593.
- Briggs, M.J., Synolakis, C.E., Kanoglu, U., & Green, D.R., 1996. Runup of solitary waves on a vertical wall. In: Yeh, H.H.J., Liu, P.L.F., Synolakis, C.E. (Eds.), *Long-wave runup models*. World Scientific, Singapore, pp. 375–383.
- Bryant, E., 2014. *Tsunamis: the underrated hazard*. third ed. Springer, Chichester, UK.
- Capone, T., Panizzo, A., & Monaghan, J.J., 2010. SPH modelling of water waves generated by submarine landslides. *J. Hydraul. Res.* 48, 80–84.
- Chen, J., Huang, Z., Jiang, C., Deng, B., & Long, Y., 2013. Tsunami-induced scour at coastal roadways: a laboratory study. *Nat. Hazards* 69, 655–674.
- Crespo, A.J.C., Gómez-Gesteira, M., & Dalrymple, R.A., 2007. Boundary conditions generated by dynamic particles in SPH methods. *Comput. Mater. Con.* 5, 173–184.
- Dalrymple, R.A., & Knio, O., 2000. SPH modelling of water waves. *Coastal Dynamics 01*. ASCE, pp. 779–787.
- Dalrymple, R.A., & Rogers, B.D., 2006. Numerical modeling of water waves with the SPH method. *Coast. Eng.* 53, 141–147.
- Edge, B.L., Gamiel, K., Dalrymple, R.A., Hérault, A., & Bilotta, G., 2014. Application of GPUSPH to design of wave energy. *Proceedings of the 9th International SPHERIC Workshop*, Paris, France, pp. 342–347.
- Farahani, R.J., & Dalrymple, R.A., 2014. Three-dimensional reversed horseshoe vortex structures under broken solitary waves. *Coast. Eng.* 91, 261–279.
- Farahani, R.J., Dalrymple, R.A., Hérault, A., & Bilotta, G., 2013. Three-dimensional SPH modeling of a bar/rip channel system. *J. Waterw. Port Coast. Ocean Eng.* 140, 82–99.
- Fenton, J.D., 2003. The effects of obstacles on surface levels and boundary resistance in open channels. *Proceedings of 30th IAHR Congress*, pp. 9–16.
- Gómez-Gesteira, M., & Dalrymple, R.A., 2004. Using a three-dimensional Smoothed Particle Hydrodynamics method for wave impact on a tall structure. *J. Waterw. Port Coast. Ocean Eng.* 130, 63–69.
- Hérault, A., Bilotta, G., & Dalrymple, R.A., 2010. SPH on GPU with CUDA. *J. Hydraul. Res.* 48, 74–79.
- Hérault, A., Bilotta, G., Vicari, A., Rustico, E., & Del Negro, C., 2011. Numerical simulation of lava flow using a GPU SPH model. *Ann. Geophys.* 54.
- Hérault, A., Bilotta, G., & Dalrymple, R.A., 2014. Achieving the best accuracy in an SPH implementation. *Proceedings of the 9th International SPHERIC Workshop*, Paris, France, pp. 134–139.
- Kawashima, K., & Buckle, I., 2013. Structural performance of bridges in the Tohoku-Oki earthquake. *Earthquake Spectra* 29, S315–S338.
- Kawashima, K., Kosa, K., Takahashi, Y., Akiyama, M., Nishioka, T., Watanabe, G., Koga, H., & Matsuzaki, H., 2011. Damages of bridges during 2011 Great East Japan Earthquake. *Proceedings of 43rd Joint Meeting, US-Japan Panel on Wind and Seismic Effects*, UJNR Tsukuba Science City, Japan.
- Matsuyama, M., & Tanaka, H., 2001. An experimental study of the highest run-up height in the 1993 Hokkaido Nansei-oki earthquake tsunami. *National Tsunami Hazard Mitigation Program Review and International Tsunami Symposium (ITS)*, pp. 879–889.
- Monaghan, J.J., 1992. Smoothed Particle Hydrodynamics. *Annu. Rev. Astron. Astrophys.* 30, 543–574.
- Monaghan, J.J., 1994. Simulating free surface flows with SPH. *J. Comput. Phys.* 110, 399–406.
- Monaghan, J.J., & Kos, A., 1999. Solitary waves on a cretan beach. *J. Waterw. Port Coast. Ocean Eng.* 125, 145–155.
- NVIDIA, 2014. *CUDA C Programming Guide 6.5*. Technical Report. NVIDIA Corporation, USA.
- Ramsden, J.D., & Raichlen, F., 1990. Forces on vertical wall caused by incident bores. *J. Waterw. Port Coast. Ocean Eng.* 116, 592–613.
- Rogers, B.D., & Dalrymple, R.A., 2008. SPH modeling of tsunami waves. *Adv. Coast. Ocean Eng.* 10, 75–100.
- Rueben, M., Cox, D., Holman, R., Shin, S., & Stanley, J., 2014. Optical measurements of tsunami inundation and debris movement in a large-scale wave basin. *J. Waterw. Port Coast. Ocean Eng.* 141.
- Rustico, E., Bilotta, G., Gallo, G., Hérault, A., & Del Negro, C., 2012. Smoothed Particle Hydrodynamics simulations on multi-GPU systems. *2012 20th Euromicro International Conference on Parallel, Distributed and Network-Based Processing, IEEE, Garching/Munich, Germany*, pp. 384–391.
- Saatcioglu, M., Ghobarah, A., & Nistor, I., 2006. Performance of structures in Indonesia during the December 2004 great Sumatra earthquake and Indian Ocean tsunami. *Earthquake Spectra* 22, 295–319.
- Shadloo, M.S., Weiss, R., Yildiz, M., & Dalrymple, R.A., 2015. Numerical simulation of long wave runup for breaking and nonbreaking waves. *Int. J. Offshore Polar Eng.* 25, 1–7.
- Smagorinsky, J., 1963. General circulation experiments with the primitive equations: I. the basic experiment. *Mon. Weather Rev.* 91, 99–164.
- St-Germain, P., Nistor, I., Townsend, R., & Shibayama, T., 2014. Smoothed-particle hydrodynamics numerical modeling of structures impacted by tsunami bores. *J. Waterw. Port Coast. Ocean Eng.* 140, 66–81.
- Swigler, D.T., 2009. *Laboratory study investigating the three dimensional turbulence and kinematic properties associated with a breaking solitary wave* (Master's thesis) Texas A&M University, USA.
- Tanaka, H., Tinh, N.X., Umeda, M., Hirao, R., Pradjoko, E., Mano, A., & Udo, K., 2012. Coastal and estuarine morphology changes induced by the 2011 Great East Japan Earthquake Tsunami. *Coast. Eng.* 54.
- Titov, V.V., & Synolakis, C.E., 1995. Modeling of breaking and nonbreaking long-wave evolution and runup using VTCS-2. *J. Waterw. Port Coast. Ocean Eng.* 121, 308–316.
- Tonkin, S., Yeh, H., Kato, F., & Sato, S., 2003. Tsunami scour around a cylinder. *J. Fluid Mech.* 496, 165–192.
- Wei, Z., & Jia, Y., 2014. Simulation of nearshore wave processes by a depth-integrated non-hydrostatic finite element model. *Coast. Eng.* 83, 93–107.
- Weiss, R., Munoz, A.J., Dalrymple, R.A., Hérault, A., & Bilotta, G., 2010. Three-dimensional modeling of long-wave runup: simulation of tsunami inundation with GPU-SPHYSICS. In: Smith, J.M., Lynett, P. (Eds.), *Proc. 32nd International Conference on Coastal Engineering*.
- Wendland, H., 1995. Piecewise polynomial, positive definite and compactly supported radial functions of minimal degree. *Adv. Comput. Math.* 4, 389–396.
- Yeh, H., & Mason, H.B., 2013. Sediment response to tsunami loading: mechanisms and estimates. *Geotechnique* 64, 131–143.
- Yeh, H., Robertson, I., & Preuss, J., 2005. *Development of design guidelines for structures that serve as tsunami vertical evacuation sites vol. 4*. Washington State Department of Natural Resources, Division of Geology and Earth Resources.